Frequency Splitting of Chiral Phonons from Broken Time-Reversal Symmetry in CrI$_3$

John Bonini,[1] Shang Ren,[2] David Vanderbilt,[2] Massimiliano Stengel,[3,4] Cyrus E. Dreyer,[5,1] and Sinisa Coh[6]

[1]Center for Computational Quantum Physics, Flatiron Institute, 162 5th Avenue, New York, New York 10010, USA
[2]Department of Physics and Astronomy, Rutgers University, Piscataway, New Jersey 08845-0849, USA
[3]Institut de Ciència de Materials de Barcelona (ICMAB-CSIC), Campus UAB, 08193 Bellaterra, Spain
[4]ICREA-Institució Catalana de Recerca i Estudis Avançats, 08010 Barcelona, Spain
[5]Department of Physics and Astronomy, Stony Brook University, Stony Brook, New York 11794-3800, USA
[6]Materials Science and Mechanical Engineering, University of California, Riverside, California 92521, USA

Conventional approaches for lattice dynamics based on static interatomic forces do not fully account for the effects of time-reversal-symmetry breaking in magnetic systems. Recent approaches to rectify this involve incorporating the first-order change in forces with atomic velocities under the assumption of adiabatic separation of electronic and nuclear degrees of freedom. In this Letter, we develop a first-principles method to calculate this velocity-force coupling in extended solids and show via the example of ferromagnetic CrI$_3$ that, due to the slow dynamics of the spins in the system, the assumption of adiabatic separation can result in large errors for splittings of zone-center chiral modes. We demonstrate that an accurate description of the lattice dynamics requires treating magnons and phonons on the same footing.

The atomic vibrations that are present in molecules and solids play a crucial role in their thermodynamic and transport properties. First-principles calculations based on density-functional theory (DFT) have been established as a powerful tool for understanding and predicting lattice-dynamical properties, including phonon dispersion [1,2] and electron-phonon coupling [3,4]. The key quantity underlying such calculations is the interatomic force constant (IFC) matrix, which is constructed by finding derivatives of the nuclear forces with respect to nuclear positions, either directly via finite displacements or through density-functional perturbation theory [1,2].

In the presence of magnetic ordering, the change in the electronic ground state compared to the nonmagnetic case propagates to the IFCs [5–9]. However, since it is defined and calculated as a static response function, the IFC matrix is invariant under time reversal by construction. Thus, a description of the nuclear dynamics based solely on the IFCs will not correctly reflect the vibration mode degeneracies in a magnetic system; instead, the phonon frequency spectrum will be determined by the *nonmagnetic* symmetry group.

There has been significant recent work on the explicit inclusion of time-reversal-symmetry (TRS) breaking in the nuclear equations of motion via the *velocity* dependence of the interatomic forces, applied to models [10–13] and magnetic molecules [14]. This "velocity-force" coupling can be obtained from the nuclear Berry curvature, which describes the evolution of the phase of the electronic wave function with changes in nuclear coordinates [10,11,14]. A key result of including this coupling

is that degenerate vibrational modes may split into non-degenerate chiral modes [15] with a well-defined finite angular momentum [14,16], even at the Brillouin-zone center. Thus, the correct treatment of magnetic symmetry is crucial for elucidating the role of atomic vibrations in thermal Hall [11,17–20] and other effects involving TRS-broken lattice dynamics [15,21–27].

A key assumption underlying the velocity-force approach in previous works [10–14] is that the timescale for electronic dynamics is fast compared to nuclear dynamics. However, this may completely break down in some systems [28], e.g., when the nuclear Berry curvature results from nuclei coupling to *spins*, whose dynamics are not necessarily faster than the atomic vibrations. The breakdown of the adiabatic picture could have a profound effect on the predicted splitting of chiral phonon modes.

In this Letter, we illustrate such a situation using the bulk-layered magnetic insulator CrI$_3$ as an example system. We first develop a DFT methodology amenable to both molecules and solids for computing phonons in the presence of velocity-force coupling. We apply this method to calculate the zone-center phonons in CrI$_3$ and show that the velocity-force response is dominated by the canting of the spins on the Cr sites caused by atomic displacements. Such spin canting has relatively slow dynamics (characterized by the zone-center magnons [29–36]). With a minimal model, we show that treating spins and atomic displacements on the same footing is necessary to avoid large errors in the frequency splitting of the chiral modes.

We begin by reviewing the formalism of the velocity-force coupling from previous works [10–14], which we will

refer to as the "Mead-Truhlar" (MT) approach. (In order to simplify the discussion, we initially assume a finite system.) The starting point of the derivation is the Born-Oppenheimer approximation, where the system wave function is factored into nuclear and electronic parts such that the ground-state electronic wave function $|\psi(\mathbf{R})\rangle$ depends parametrically on the nuclear coordinates $\mathbf{R}$ [37]. Once the electronic degrees of freedom are integrated out, the effective nuclear Hamiltonian becomes [13]

$$H_{\text{eff}} = \sum_{i\alpha} \frac{[p_{i\alpha} - \hbar A_{i\alpha}(\mathbf{R})]^2}{2m_i} + V_{\text{eff}}(\mathbf{R}), \qquad (1)$$

where Roman indices (here, i) run over nuclei, Greek indices (here, α) run over Cartesian directions, $p_{i\alpha}$ is the momentum operator for nucleus i along direction α, and m_i is the mass of nucleus i. Using the notation $\partial_{i\alpha} = \partial/\partial R_{i\alpha}$, $A_{i\alpha}(\mathbf{R}) = i\langle\psi(\mathbf{R})|\partial_{i\alpha}\psi(\mathbf{R})\rangle$ is a nuclear Berry potential, and $V_{\text{eff}}(\mathbf{R}) = \epsilon(\mathbf{R}) + \sum_{i\alpha}(\hbar^2/2m_i)[\langle\partial_{i\alpha}\psi(\mathbf{R})|\partial_{i\alpha}\psi(\mathbf{R})\rangle - A_{i\alpha}(\mathbf{R})^2]$ is an effective scalar potential, where $\epsilon(\mathbf{R})$ is the ground-state energy for a given fixed nuclear configuration. As first pointed out by Mead and Truhlar [13], the nuclear Berry potential $A_{i\alpha}$ cannot always be made to vanish by changing the gauge of $|\psi(\mathbf{R})\rangle$ via the choice of an $\mathbf{R}$-dependent phase factor.

The resulting vibrational modes are then found by solving the equations of motion which, to harmonic order in nuclear displacements, are given by [10–13]

$$\omega_n^2 \mathbf{M}\eta_n = (\mathbf{C} + i\omega_n\mathbf{G})\eta_n. \qquad (2)$$

Here, $\mathbf{M}$ is a diagonal nuclear mass matrix $M_{i\alpha,j\beta} = m_i\delta_{i,j}\delta_{\alpha,\beta}$, ω_n is the frequency of mode n, and $\eta_n(j\alpha)$ is the component of the eigendisplacement of nucleus j along direction α normalized so that $\eta_n^\dagger\mathbf{M}\eta_m = \delta_{nm}$. $\mathbf{G}$ is the "velocity-force matrix," whose elements $G_{i\alpha,j\beta}$ relate the force on nucleus i along direction α to the velocity of nucleus j along direction β, and are expressed as

$$G_{i\alpha,j\beta} = -2\hbar\,\text{Im}\langle\partial_{i\alpha}\psi(\mathbf{R})|\partial_{j\beta}\psi(\mathbf{R})\rangle, \qquad (3)$$

which is just $\hbar$ times the nuclear Berry curvature. The matrix $\mathbf{C}$ is the IFC matrix, which we define to be $C_{i\alpha,j\beta} = \partial_{i\alpha}\partial_{j\beta}\epsilon(\mathbf{R})$. Note that following Eq. (1) one could alternatively define $\mathbf{C}$ in terms of the Hessian of V_{eff}, which includes additional terms compared to the conventional IFC. However, the additional terms are higher order in the inverse nuclear mass and do not involve breaking of time-reversal symmetry, so we neglect them in this Letter.

This formalism can be extended to the calculation of phonons in infinite crystals within DFT. In Sec. S1 of Supplemental Material [38], which includes Ref. [39], we describe our approach, focusing on zone-center phonon modes and utilizing finite-displacement DFT calculations

to obtain the Berry curvature in Eq. (3). Additional computational details can be found in Sec. S5 [38], which includes Refs. [40–45].

We now present results for zone-center phonons in the ferromagnetic state of CrI_3. As mentioned above, the conventional calculation of phonons neglects $\mathbf{G}$ in Eq. (2), resulting in an equation of motion with TRS ($\tilde{\omega}_n^2\mathbf{M}\tilde{\eta}_n = \mathbf{C}\tilde{\eta}_n$). The resulting zone-center phonon modes with frequencies $\tilde{\omega}_n$ can be represented with real eigendisplacements $\tilde{\eta}_n$. In CrI_3, the representation of these modes at the zone center can be decomposed into the real irreducible representations (irreps) of $\bar{3}$ as $4A_g \oplus 4A_u \oplus 4E_g \oplus 4E_u$. The frequencies $\tilde{\omega}_n$ range up to 32 meV (see Supplemental Material [38], Table SIII). We can consider the velocity-force coupling between phonon modes obtained from the IFC alone by defining $\bar{G}_{nm} = \tilde{\eta}_n^\dagger\mathbf{G}\tilde{\eta}_m$; $\bar{\mathbf{G}}$ is block diagonal, with each block corresponding to a real irrep. Once $\mathbf{G}$ is included in Eq. (2), TRS is broken and the twofold-degenerate E_u and E_g modes split, as the corresponding irreps further break up into complex one-dimensional representations.

In Fig. 1(b), we show a selection of zone-center phonon frequencies of bulk ferromagnetic CrI_3 (see Supplemental Material [38] Table SIII for a complete list of frequencies). On the left side, we plot the frequencies neglecting the velocity-force contribution and on the right the frequencies
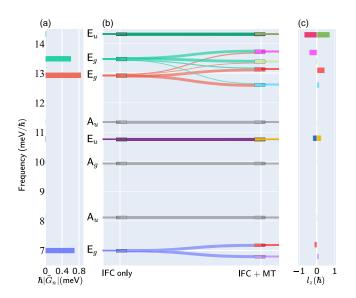

FIG. 1. For selected zone-center phonon modes of bulk ferromagnetic CrI_3: (a) norm of the row of the velocity-force matrix $\bar{\mathbf{G}}$ relevant to each phonon mode; (b) phonon frequencies (labeled by irreducible representation) determined from just the interatomic force-constant matrix on the left of the panel ("IFC only"), and including the Mead-Truhlar correction on the right side ("IFC + MT"), illustrating the frequency splitting of degenerate modes; and (c) angular momentum values of each mode after the velocity-force matrix contributions have been included. In (b), the thickness of the connection between modes corresponds to the magnitude of the overlap between their respective eigenvectors (curvature of lines is arbitrary).

including the velocity-force contribution via the MT approach. The splitting of the twofold-degenerate modes due to the inclusion of the **G** matrix results in phonons with well-defined angular momentum in the z direction (due to the symmetry of CrI_3), shown in Fig. 1(c). (See Sec. S4 [38] for a full analysis, which includes Refs. [46]). In Fig. 1(a), we plot the sum of the magnitudes of the velocity-force coupling terms relevant to each phonon eigenvector, as a measure of the strength of the coupling. We see that the E_g modes have the strongest coupling. We shall see why shortly.

We now analyze the mechanisms responsible for the velocity-force coupling in CrI_3. The magnetic moments reside on the Cr atoms and are initially oriented out of plane along z. The modes with large $\bar{\mathbf{G}}$ matrix elements in Fig. 1 are those mostly involving displacements of the I sublattices, which carry strong spin-orbit coupling. Under such displacements, it is natural that the Cr moments may cant, reflecting a local change in magnetic easy axis. This canting will result in a spin Berry curvature and, thus, a contribution to **G**.

In fact, we find that, for CrI_3, the spin Berry curvature is the dominant mechanism of velocity-force coupling. We demonstrate this by calculating the matrix elements of **G** under the assumption that *only* the spin-Berry-curvature mechanism is present. In this "spin-Berry approximation," **G** is given by (see Sec. S1 B [38])

$$\bar{G}_{nm} = -S\sum_{Iab}\epsilon_{ab}B_{Ia,n}B_{Ib,m}, \qquad (4)$$

where we take $S = 3/2\hbar$, ϵ_{ab} is the two-dimensional Levi-Civita symbol, and $B_{Ia,n} = \partial s_{Ia}/\partial\tilde{u}_n$ is a "spin-canting matrix" describing the static change in the equilibrium spin unit vector on magnetic Cr site I in direction a resulting from phonon perturbation n ($\tilde{u}_n$ is the amplitude of mode n).

A comparison between this spin-Berry approximation and the full Berry-phase calculation of the **G** matrix is presented in Table SII [38]. Across all phonon modes, the error in the frequency splitting predicted by the spin-Berry approximation is less than 0.016 meV. For the E_g modes, this error is under 0.006 meV. For the modes where splitting is significant (greater than 0.1 meV), the splittings in the spin-Berry approximation differ from the full MT approach by less than 1%.

This is a remarkable result and is one of the main findings of the present Letter. By adopting the spin-Berry approximation, only information about the spin canting in response to phonon distortions is needed to compute **G**. It is now clear why the **G** tensor elements are so much smaller for the E_u modes; these are the ones that couple to the optical magnons, whose much larger stiffness strongly suppresses the spin canting.

A critical implication of the fact that the velocity-force coupling in CrI_3 results from spin canting is that the assumption underlying the MT approach of Eqs. (1)–(3), namely, that all electronic dynamics are fast compared to that of the phonons, is clearly unfounded. This is because the relevant timescale for spin dynamics is that of the magnon frequencies in the system. The experimentally measured zone-center magnons of CrI_3 have frequencies of 0.3 meV for the acoustic branch and 17 meV for the optical branch [36], while the relevant phonons with the largest velocity-force coupling have frequencies in the range of 6–14 meV [see Fig. 1(b)].

Thus, an appropriate description of the low-energy dynamics must treat spins and phonons in this system on the same footing. To illustrate how this can be done, we focus on a single pair of E_g or E_u modes, which couple, respectively, to either an effective acoustic spin unit vector $\mathbf{s} = (\mathbf{s}_1 + \mathbf{s}_2)/\sqrt{2}$ or its optical counterpart $\mathbf{s} = (\mathbf{s}_1 - \mathbf{s}_2)/\sqrt{2}$. Denoting the phonon mode amplitudes and momenta as (x, y) and (p_x, p_y), respectively, the coupled spin-phonon Hamiltonian takes the form

$$H = \frac{1}{2}(p_x^2 + p_y^2) + \frac{1}{2}\tilde{\omega}^2(x^2 + y^2)$$
$$+ \frac{1}{2}\alpha(s_x^2 + s_y^2) + \gamma(xs_x + ys_y). \qquad (5)$$

Here, $\tilde{\omega}$ is the bare phonon frequency, $\alpha = \partial^2 E/\partial^2 s_x$ is the spin anisotropy energy, and $\gamma = \partial^2 E/\partial x\partial s_x$ is the coupling between the spin and the pair of phonons. Note that the unperturbed magnon frequency is related to the anisotropy by $\omega_m = \alpha/S$, where $S = 3\hbar/2$ is the Cr spin, and that the **B** matrix introduced above reduces in this minimal model to $B = \gamma/\alpha$.

Going over to circularly polarized coordinates via $x_\pm = (x \pm iy)/\sqrt{2}$ and $s_\pm = (s_x \pm is_y)/\sqrt{2}$, the equations of motion become

$$(\tilde{\omega}^2 - \omega^2)x_\pm = -\gamma s_\pm,$$
$$(\pm\omega_m - \omega)s_\pm = \mp S^{-1}\gamma x_\pm, \qquad (6)$$

which are easily solved numerically. Further details on the spin-phonon model are presented in Sec. S6 [38], which includes Ref. [47].

In Table I, we compare the frequency splittings of doubly degenerate modes determined by the adiabatic MT approach and spin-phonon (SP) model. The last column in Table I presents the results for the spin-phonon model; the E_g modes couple to the acoustic magnon branch and the E_u modes to the optical branch. Though *ab initio* methods for computing magnon frequencies exist [30,35,48–50], we use experimental magnon frequencies of 0.3 (acoustic) and 17 meV (optical), from Ref. [36]. A more detailed

TABLE I. Frequency splitting of E_u and E_g zone-center phonon modes in CrI$_3$. Modes are labeled by their symmetry and frequency determined only from the interatomic force constants ($\hbar\tilde{\omega}$). MT refers to frequency splittings obtained by solving the equation of motion in Eq. (2), and SP corresponds to solving the coupled equations of motion in Eq. (6).

Irrep	$\hbar\tilde{\omega}$ (meV)	Splitting (meV)	
		MT	SP
E_g	6.9999	0.3820	0.0007
	12.9287	0.5270	0.0003
	13.4876	0.3368	0.0001
	29.8521	0.0244	3×10^{-6}
E_u	10.7667	0.0043	0.0046
	14.3259	0.0090	0.0311
	27.8168	0.0349	0.0118

comparison of the Mead-Truhlar approach and spin-phonon model is presented in Sec. S3 [38], which includes Ref. [51].

To understand the general features of the spin-phonon mixing, we plot in Fig. 2 the solutions of Eq. (6) as a function of phonon frequency $\tilde{\omega}$, with the magnon frequency set to optical branch $\omega_m = 17$ meV/$\hbar$ [36] and γ fixed at 2 meV$^{3/2}$/$\hbar$, a typical value for the E_u modes in CrI$_3$ (since those modes couple to the optical magnon). The solid blue curve in the inset shows the splitting of the modes with dominant phonon character also as a function of $\tilde{\omega}$. Outside of the small "resonant" regime $\tilde{\omega} \simeq \omega_m$, where significant magnon-phonon hybridization occurs, the mode splitting is well described by SB^2F (see the orange dashed curve in the inset in Fig. 2), where SB^2 is the relevant velocity-force term in the adiabatic spin-Berry approximation [i.e., Eq. (4)] and $F = |1 - (\tilde{\omega}/\omega_m)^2|^{-1}$. At small $\tilde{\omega}$, the magnon can be treated as a high-energy degree
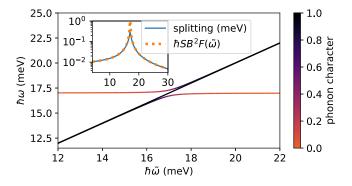

FIG. 2. Frequencies of interacting magnons and phonons as given by Eq. (6) as a function of uncoupled phonon frequency ($\tilde{\omega}$) for $\omega_m = 17$ meV/$\hbar$ and $\gamma = 2$ meV$^{3/2}$/$\hbar$ which corresponds to a velocity-force matrix element of $\bar{G} = 0.01$ meV/$\hbar$. The color of the curve indicates the magnitude of the phonon component of the mode eigenvector. The inset shows the splitting of the modes as well as the heuristic for splitting away from resonance, $\hbar SB^2F(\tilde{\omega})$, where $F = |1 - (\tilde{\omega}/\omega_m)^2|^{-1}$.

of freedom which renormalizes the phonons, and the splitting from the MT approach is recovered. Increasing $\tilde{\omega}$ toward ω_m enhances the splitting of modes over the value at the adiabatic (MT) limit, peaking at the point where the magnon and phonon frequencies coincide and the modes have maximum hybridization. Above ω_m, the splitting decreases from its peak value but is still enhanced over that determined by the MT approach for a range of $\tilde{\omega}$. At $\tilde{\omega} \gg \omega_m$, the splitting is suppressed and vanishes as $\tilde{\omega} \to \infty$.

This behavior is reflected in the splittings given in Table I. Two of the three E_u modes which couple to the optical magnon have frequencies below $\omega_m = 17$ meV/$\hbar$ but still in ranges where the splitting is enhanced above the adiabatic MT limit, as the phonons are becoming hybridized with the magnon instead of just having their frequencies renormalized by it. However, since the splittings in the adiabatic limit (and, thus, the corresponding **G** matrix elements) are proportional to ω_m^{-2}, the splittings remain quite small. The largest frequency E_u mode has $\omega_m \ll \tilde{\omega}$, so that the splitting is reduced compared to values obtained from the velocity-force approach.

The E_g modes couple to the acoustic magnon ($\omega_m = 0.3$ meV/$\hbar$), so for all E_g modes $\tilde{\omega} \gg \omega_m$, which is precisely the opposite of the limit in which the adiabatic velocity-force theory is applicable. This results in the drastic reduction ($F \ll 1$) in the splitting of the E_g modes in Table I compared to the MT description in Eq. (2). The physical interpretation of this regime is that the Cr spins cannot keep up with the phonons, and, thus, the area swept out from the spin canting is greatly reduced compared to the assumption that they follow the nuclear motion adiabatically.

Clearly, these results have significant implications for experimental measurements of chiral phonons in CrI$_3$. Optical techniques, possibly using circular polarization, constitute a powerful tool for studying such properties [21,24,52–54]. The strongly suppressed frequency splitting (SP column in Table I) of the Raman-active E_g modes is likely to be difficult to detect. This is consistent with recent work on CrBr$_3$, which found signatures of the chiral phonons but did not report a splitting of these modes [24]. The larger, though still quite modest, splitting of the E_u modes could, in principle, be measured by peak shifts in infrared absorption [55], while direct detection of chirality would require circularly polarized infrared spectroscopy as in Refs. [52,53].

More generally, our results also have several implications for finding other systems with a large splitting of chiral phonon modes at Γ. In materials like CrI$_3$, where the spin-Berry mechanism is responsible for the majority of the velocity-force coupling, it is most promising to look for (or engineer via, e.g., strain or magnetic field) cases where the relevant phonon and magnon frequencies coincide. This avoids the suppression of the splitting in the $\tilde{\omega} \gg \omega_m$

regime and the small spin canting likely when $\omega_m \gg \tilde{\omega}$. Systems with lower-frequency optical magnons that maintain similar or larger spin-phonon coupling γ are also strong candidates for observing larger effects. In any case, we can see from Table I that correctly accounting for the relative dynamics of spins versus phonons is necessary to avoid significantly overestimating the splitting of certain chiral modes.

In conclusion, we have developed a first-principles methodology for capturing time-reversal-symmetry-broken lattice dynamics in magnetic solids and, via the example of ferromagnetic CrI_3, demonstrated that the previously made assumption of fast electron dynamics compared to the lattice may break down. Using a minimal model, we show that spins and phonons must be treated on equal footing to avoid large qualitative errors in the splitting of chiral modes.

[1] Xavier Gonze and Changyol Lee, Dynamical matrices, Born effective charges, dielectric permittivity tensors, and interatomic force constants from density-functional perturbation theory, Phys. Rev. B **55**, 10355 (1997).

[2] Stefano Baroni, Stefano de Gironcoli, Andrea Dal Corso, and Paolo Giannozzi, Phonons and related crystal properties from density-functional perturbation theory, Rev. Mod. Phys. **73**, 515 (2001).

[3] Feliciano Giustino, Electron-phonon interactions from first principles, Rev. Mod. Phys. **89**, 015003 (2017).

[4] Bartomeu Monserrat, Electron-phonon coupling from finite differences, J. Phys. Condens. Matter **30**, 083001 (2018).

[5] Michel Posternak, Alfonso Baldereschi, Sandro Massidda, and Nicola Marzari, Maximally localized Wannier functions in antiferromagnetic MnO within the FLAPW formalism, Phys. Rev. B **65**, 184422 (2002).

[6] Jun Hee Lee and Karin M. Rabe, Large spin-phonon coupling and magnetically induced phonon anisotropy in SrMO_3 perovskites (M = V,Cr,Mn,Fe,Co), Phys. Rev. B **84**, 104440 (2011).

[7] Jiawang Hong, Alessandro Stroppa, Jorge Íñiguez, Silvia Picozzi, and David Vanderbilt, Spin-phonon coupling effects in transition-metal perovskites: A DFT $+ U$ and hybrid-functional study, Phys. Rev. B **85**, 054417 (2012).

[8] Ke Wang, WuXing Zhou, Yuan Cheng, Min Zhang, Hai Wang, and Gang Zhang, Magnetic order-dependent phonon properties in 2D magnet CrI_3, Nanoscale **13**, 10882 (2021).

[9] Jiangbin Wu, Yu Yao, Miao-Ling Lin, Malte Rösner, Zhonghao Du, Kenji Watanabe, Takashi Taniguchi, Ping-Heng Tan, Stephan Haas, and Han Wang, Spin–phonon coupling in ferromagnetic monolayer chromium tribromide, Adv. Mater. **34**, 2108506 (2022).

[10] Tao Qin, Jianhui Zhou, and Junren Shi, Berry curvature and the phonon Hall effect, Phys. Rev. B **86**, 104305 (2012).

[11] Takuma Saito, Kou Misaki, Hiroaki Ishizuka, and Naoto Nagaosa, Berry Phase of Phonons and Thermal Hall Effect in Nonmagnetic Insulators, Phys. Rev. Lett. **123**, 255901 (2019).

[12] Daniyar Saparov, Bangguo Xiong, Yafei Ren, and Qian Niu, Lattice dynamics with molecular Berry curvature: Chiral optical phonons, Phys. Rev. B **105**, 064303 (2022).

[13] C. Alden Mead and Donald G. Truhlar, On the determination of Born-Oppenheimer nuclear motion wave functions including complications due to conical intersections and identical nuclei, J. Chem. Phys. **70**, 2284 (1979).

[14] Oliviero Bistoni, Francesco Mauri, and Matteo Calandra, Intrinsic Vibrational Angular Momentum from Nonadiabatic Effects in Noncollinear Magnetic Molecules, Phys. Rev. Lett. **126**, 225703 (2021).

[15] Lifa Zhang and Qian Niu, Angular Momentum of Phonons and the Einstein–de Haas Effect, Phys. Rev. Lett. **112**, 085503 (2014).

[16] Sinisa Coh, Classification of materials with phonon angular momentum and microscopic origin of angular momentum, arXiv:1911.05064.

[17] G. Grissonnanche, A. Legros, S. Badoux, E. Lefrançois, V. Zatko, M. Lizaire, F. Laliberté, A. Gourgout, J. S. Zhou, S. Pyon, T. Takayama, H. Takagi, S. Ono, N. Doiron-Leyraud, and L. Taillefer, Giant thermal Hall conductivity in the pseudogap phase of cuprate superconductors, Nature (London) **571**, 376 (2019).

[18] Jing-Yuan Chen, Steven A. Kivelson, and Xiao-Qi Sun, Enhanced Thermal Hall Effect in Nearly Ferroelectric Insulators, Phys. Rev. Lett. **124**, 167601 (2020).

[19] Xiaokang Li, Benoît Fauqué, Zengwei Zhu, and Kamran Behnia, Phonon Thermal Hall Effect in Strontium Titanate, Phys. Rev. Lett. **124**, 105901 (2020).

[20] Heda Zhang, Chunqiang Xu, Caitlin Carnahan, Milos Sretenovic, Nishchay Suri, Di Xiao, and Xianglin Ke, Anomalous Thermal Hall Effect in an Insulating van der Waals Magnet, Phys. Rev. Lett. **127**, 247202 (2021).

[21] Hanyu Zhu, Jun Yi, Ming-Yang Li, Jun Xiao, Lifa Zhang, Chih-Wen Yang, Robert A. Kaindl, Lain-Jong Li, Yuan Wang, and Xiang Zhang, Observation of chiral phonons, Science **359**, 579 (2018).

[22] Hao Chen, Wei Zhang, Qian Niu, and Lifa Zhang, Chiral phonons in two-dimensional materials, 2D Mater. **6**, 012002 (2018).

[23] J. H. Mentink, M. I. Katsnelson, and M. Lemeshko, Quantum many-body dynamics of the Einstein–de Haas effect, Phys. Rev. B **99**, 064428 (2019).

[24] Tingting Yin, Kanchan Ajit Ulman, Sheng Liu, Andrés Granados del Águila, Yuqing Huang, Lifa Zhang, Marco Serra, David Sedmidubsky, Zdenek Sofer, Su Ying Quek, and Qihua Xiong, Chiral phonons and giant magneto-optical effect in $CrBr_3$ 2D magnet, Adv. Mater. **33**, 2101618 (2021).

[25] Hao Chen, Weikang Wu, Jiaojiao Zhu, Zhengning Yang, Weikang Gong, Weibo Gao, Shengyuan A. Yang, and Lifa Zhang, Chiral phonon diode effect in chiral crystals, Nano Lett. **22**, 1688 (2022).

[26] Andrey Baydin, Felix G. G. Hernandez, Martin Rodriguez-Vega, Anderson K. Okazaki, Fuyang Tay, G. Timothy Noe, Ikufumi Katayama, Jun Takeda, Hiroyuki Nojiri, Paulo H. O. Rappl, Eduardo Abramof, Gregory A. Fiete, and Junichiro Kono, Magnetic Control of Soft Chiral Phonons in PbTe, Phys. Rev. Lett. **128**, 075901 (2022).

[27] Dominik M. Juraschek, Tomáš Neuman, and Prineha Narang, Giant effective magnetic fields from optically driven chiral phonons in $4f$ paramagnets, Phys. Rev. Res. **4**, 013129 (2022).

[28] Anna Miglio, Véronique Brousseau-Couture, Emile Godbout, Gabriel Antonius, Yang-Hao Chan, Steven G. Louie, Michel Côté, Matteo Giantomassi, and Xavier Gonze, Predominance of non-adiabatic effects in zero-point renormalization of the electronic band gap, npj Comput. Mater. **6**, 1 (2020).

[29] Wei-Bing Zhang, Qian Qu, Peng Zhu, and Chi-Hang Lam, Robust intrinsic ferromagnetism and half semiconductivity in stable two-dimensional single-layer chromium trihalides, J. Mater. Chem. C **3**, 12457 (2015).

[30] J L Lado and J Fernández-Rossier, On the origin of magnetic anisotropy in two dimensional CrI_3, 2D Mater. **4**, 035002 (2017).

[31] Lucas Webster and Jia-An Yan, Strain-tunable magnetic anisotropy in monolayer $CrCl_3$, $CrBr_3$, and CrI_3, Phys. Rev. B **98**, 144411 (2018).

[32] Nils Richter, Daniel Weber, Franziska Martin, Nirpendra Singh, Udo Schwingenschlögl, Bettina V. Lotsch, and Mathias Kläui, Temperature-dependent magnetic anisotropy in the layered magnetic semiconductors CrI_3 and $CrBr_3$, Phys. Rev. Mater. **2**, 024004 (2018).

[33] Inhee Lee, Franz G. Utermohlen, Daniel Weber, Kyusung Hwang, Chi Zhang, Johan van Tol, Joshua E. Goldberger, Nandini Trivedi, and P. Chris Hammel, Fundamental Spin Interactions Underlying the Magnetic Anisotropy in the Kitaev Ferromagnet CrI_3, Phys. Rev. Lett. **124**, 017201 (2020).

[34] C. Bacaksiz, D. Šabani, R. M. Menezes, and M. V. Milošević, Distinctive magnetic properties of CrI_3 and $CrBr_3$ monolayers caused by spin-orbit coupling, Phys. Rev. B **103**, 125418 (2021).

[35] Liqin Ke and Mikhail I. Katsnelson, Electron correlation effects on exchange interactions and spin excitations in 2D van der Waals materials, npj Comput. Mater. **7**, 4 (2021).

[36] John Cenker, Bevin Huang, Nishchay Suri, Pearl Thijssen, Aaron Miller, Tiancheng Song, Takashi Taniguchi, Kenji Watanabe, Michael A. McGuire, Di Xiao, and Xiaodong Xu, Direct observation of two-dimensional magnons in atomically thin CrI_3, Nat. Phys. **17**, 20 (2021).

[37] Max Born and Kun Huang, *Dynamical Theory of Crystal Lattices*, International Series of Monographs on Physics (Oxford University Press, Oxford, 1954).

[38] See Supplemental Material at http://link.aps.org/supplemental/10.1103/PhysRevLett.130.086701 for additional data, further discussion of the computed phonon angular momentum, a more explicit derivation of the

[39] David Vanderbilt, *Berry Phases in Electronic Structure Theory: Electric Polarization, Orbital Magnetization and Topological Insulators* (Cambridge University Press, Cambridge, England, 2018), Chap. 3.

[40] G. Kresse and J. Hafner, Ab initio molecular dynamics for liquid metals, Phys. Rev. B **47**, 558 (1993).

[41] G. Kresse and J. Furthmüller, Efficient iterative schemes for ab initio total-energy calculations using a plane-wave basis set, Phys. Rev. B **54**, 11169 (1996).

[42] G. Kresse and D. Joubert, From ultrasoft pseudopotentials to the projector augmented-wave method, Phys. Rev. B **59**, 1758 (1999).

[43] J. P. Perdew and Alex Zunger, Self-interaction correction to density-functional approximations for many-electron systems, Phys. Rev. B **23**, 5048 (1981).

[44] P. E. Blöchl, Projector augmented-wave method, Phys. Rev. B **50**, 17953 (1994).

[45] Hendrik J. Monkhorst and James D. Pack, Special points for Brillouin-zone integrations, Phys. Rev. B **13**, 5188 (1976).

[46] A G McLellan, Angular momentum states for phonons and a rotationally invariant development of lattice dynamics, J. Phys. C **21**, 1177 (1988).

[47] Th. W. Ruijgrok and H. Van der Vlist, On the Hamiltonian and Lagrangian formulation of classical dynamics for particles with spin, Physica (Amsterdam) **101A**, 571 (1980).

[48] Q. Niu, Xindong Wang, L. Kleinman, Wu-Ming Liu, D. M. C. Nicholson, and G. M. Stocks, Adiabatic Dynamics of Local Spin Moments in Itinerant Magnets, Phys. Rev. Lett. **83**, 207 (1999).

[49] D. M. Bylander, Qian Niu, and Leonard Kleinman, Fe magnon dispersion curve calculated with the frozen spin-wave method, Phys. Rev. B **61**, R11875 (2000).

[50] Ralph Gebauer and Stefano Baroni, Magnons in real materials from density-functional theory, Phys. Rev. B **61**, R6459 (2000).

[51] Wencan Jin, Hyun Ho Kim, Zhipeng Ye, Siwen Li, Pouyan Rezaie, Fabian Diaz, Saad Siddiq, Eric Wauer, Bowen Yang, Chenghe Li et al., Raman fingerprint of two terahertz spin wave branches in a two-dimensional honeycomb Ising ferromagnet, Nat. Commun. **9**, 1 (2018).

[52] L. A. Nafie, T. A. Keiderling, and P. J. Stephens, Vibrational circular dichroism, J. Am. Chem. Soc. **98**, 2715 (1976).

[53] R. Laiho, On the optical absorption and the magnetic circular dichroism of the transparent ferromagnet K_2CuF_4, Phys. Status Solidi (b) **69**, 579 (1975).

[54] Luojun Du, Jian Tang, Yanchong Zhao, Xiaomei Li, Rong Yang, Xuerong Hu, Xueyin Bai, Xiao Wang, Kenji Watanabe, Takashi Taniguchi, Dongxia Shi, Guoqiang Yu, Xuedong Bai, Tawfique Hasan, Guangyu Zhang, and Zhipei Sun, Lattice dynamics, phonon chirality, and spin–phonon coupling in 2d itinerant ferromagnet Fe_3GeTe_2, Adv. Funct. Mater. **29**, 1904734 (2019).

[55] Luca Tomarchio, Salvatore Macis, Lorenzo Mosesso, Loi T. Nguyen, Antonio Grilli, Mariangela Cestelli Guidi, Robert J. Cava, and Stefano Lupi, Low energy electrodynamics of CrI_3 layered ferromagnet, Sci. Rep. **11**, 23405 (2021).